A Physics-Based Crystallographic Modeling Framework for Describing the Thermal Creep Behavior of Fe-Cr Alloys

CrossMark

W. WEN, L. CAPOLUNGO, A. PATRA, and C.N. TOMÉ

In this work, a physics-based thermal creep model is developed based on the understanding of the microstructure in Fe-Cr alloys. This model is associated with a transition state theory-based framework that considers the distribution of internal stresses at sub-material point level. The thermally activated dislocation glide and climb mechanisms are coupled in the obstacle-bypass processes for both dislocation and precipitate-type barriers. A kinetic law is proposed to track the dislocation densities evolution in the subgrain interior and in the cell wall. The predicted results show that this model, embedded in the visco-plastic self-consistent framework, captures well the creep behaviors for primary and steady-state stages under various loading conditions. The roles of the mechanisms involved are also discussed.

I. INTRODUCTION

THE development and use of high-performance Cr-based steels, with superior high-temperature creep behavior, have been instrumental in improving the efficiency of thermal power plants.[1–8] Indeed, operation temperatures above 873 K (600 °C) have been reached thanks, in particular, to the use of 9 to 12 pct Cr steels as boiler tubes and steam pipes. In parallel, other high Cr steel grades such as Fe-Cr-Al and modified Grade 91 (Fe-9Cr-1Mo) additionally exhibit low swelling during irradiation. Naturally, these alloys are candidate material systems for various nuclear energy applications (e.g., cladding). Their advanced high-temperature creep properties could prolong the service life and enhance the accident tolerance of both light water reactors (LWRs) and very-high-temperature reactors (VHTRs).[9–14] Under such high temperature, stress, and irradiation environments, the materials microstructure and part geometry will degrade over time. In particular, both thermal and irradiation creep largely contribute to the degradation process. Focus is placed here on thermal creep.

Over the past two decades, a series of work has focused on the connections between the thermal creep behavior of high Cr steels and the specifics of their microstructures.[1–7,13,15,16] Following thermo-mechanical processing (e.g., tempering, tube extrusion), a polycrystalline sample will typically be textured, with most grains containing subgrain boundaries consisting of both geometrically necessary dislocations and $M_{23}C_6$

carbide (M = Cr). The latter also decorates grain boundaries. $M_{23}C_6$ carbide can stabilize the subgrain structure by obstructing the dislocation annihilation in the cell walls, and hence decelerate the growth of subgrains.[7,17] Finally, the microstructure contains an additional level of complexity as subgrains also contain carbo-nitride precipitates MX (M = V or Nb; X = C or N). In consequence, precipitation hardening and precipitation-enhanced subgrain boundary hardening have been suggested to be the most important creep strengthening mechanisms in high Cr steels.[1]

As a consequence of the complex microstructure, the creep rate is controlled by a broad spectrum of simultaneously active deformation mechanisms. Indeed, during thermal creep, plastic strain is likely to result from the activation of both diffusion creep and dislocation motion. The relative contribution of each depends on the imposed stress state, on the internal stress state, and on temperature. Vacancy-driven diffusion creep processes, such as the Nabarro–Herring creep and Coble creep, tend to play an important role in the high-temperature regime.[13,18] Shrestha et al.[13] show that diffusion creep is dominant in modified 9Cr-1Mo steel at 873 K (600 °C) with a creep stress lower than 60 MPa. General Ashby's deformation map indicates that dislocation motion becomes the dominant mechanism under lower temperature and higher stress conditions. Clearly in the dislocation creep regime, the interaction between moving dislocations and precipitates, subgrain boundaries, and other dislocations will be dominant. Interestingly, and on the basis of one dimensional models applied at the scale of the polycrystal, the processes allowing to overcome obstacles (e.g., cross-slip, climb, unzipping) are expected to exhibit distinct temperature and stress dependence.[19–22] This warrants the existence of different creep regimes each controlled by a different process. Finally, as dislocations interact with subgrain boundaries and as different

W. WEN, L. CAPOLUNGO, A. PATRA, and C.N. TOMÉ are with the Materials Science and Technology Division, Los Alamos National Laboratory, Los Alamos, NM 87545. Contact e-mail: wwen@lanl.gov

species migrate, both precipitate coarsening and sub-grain growth can be also activated.[2,6,17,23,24]

Polycrystal models can unravel the relative contribution of all dissipative processes. In an early work, Estrin and Mecking[25] developed a constitutive model assuming the average dislocation density is the sole structure factor affecting the mechanical state of the material. This model, which is a unified description for both dynamic loading and creep tests, tracks the dislocation density evolution through the Kocks–Mecking law, and a kinetic equation is proposed to determine the flow stress and strain rate. Gottstein and Argon[26] treat the dislocation density evolution in a more sophisticated way. The dislocation glide, climb, and cell wall migration are considered in the dislocation storage and dynamic recovery processes. Roters et al.[27] divided the dislocations in the cell-forming materials into three subsets: mobile dislocations in the subgrain, immobile dislocations in the subgrain, and immobile dislocations in the cell wall. An evolution law is proposed for each population taking into account the dislocation dipole and lock formation. While the aforementioned models focused mainly on the frameworks to track the evolution of dislocation populations, other body of work focuses on the details of the dislocation/obstacle bypass processes, i.e., Referenes 19, 21, 28, and 29. Xiang and Srolovitz[28] performed dislocation dynamic simulations on this subject for both penetrable and impenetrable particles, with dislocation glide, climb, and cross-slip mechanisms included. The climb velocity for the edge dislocation was determined through the climb component of Peach–Koehler force. The results show that generally the climb mechanism tends to reduce the stress required for the bypass.

The present work proposes a physics-based constitutive model, capable of simultaneously predicting the mechanical response of high Cr steels and of evaluating the contribution of each mechanism during thermal creep. In this crystal plasticity-based model, thermally activated dislocation glide and climb mechanisms are coupled. Their activation rates are determined via the use of harmonic transition state theory-based framework. Further, we propose to predict the activation of climb and explicit treatment of vacancy flux towards dislocations. The model presented, uses a recently proposed framework, to account for the distribution of internal stresses at a sub-material point scale. This added feature also allows selectively activating distinct dislocation glide and recovery processes (i.e., dislocation annihilation within subgrains and in subgrain boundaries). The constitutive law is embedded in a mean-field visco-plastic framework (VPSC).[30,31] The model is employed to predict the behavior of the modified 9Cr-1Mo alloy under thermal creep tests at various temperatures and stresses. The predicted results are in a fairly good agreement with the experimental data. Among others, it is suggested that dislocation recovery within the subgrain could play a dominant role in the strain rate evolution observed during creep tests.

The study is structured as follows. A detailed description of the proposed thermal creep model will be given in Section II including the modeling background, the formulation to determine the creep shear rate on each slip system, and a brief introduction of the VPSC framework. In Section III, the predicted thermal creep responses are presented and compared with the experimental data provided by Basirat et al.[14] for Fe-9Cr-1Mo steel under various temperatures and applied stresses. The studies on the contributions of the mechanisms and the parameter sensitivities are also proposed. Section IV presents a discussion of the role of each dislocation recovery process on the stress dependence of the creep rate.

II. MODELING FRAMEWORK

A. Microstructure and Considered Mechanisms

A paradigm microstructure, with features characteristic of high Cr alloys schematically presented in Figure 1, is chosen as the foundation of this model. This is the typical microstructure for heat-treated and thermo-mechanically processed high Cr steels.[1,3,6,13] As shown, each grain contains a number of elongated subgrains which boundaries are denoted with dotted lines. Each subgrain contains a high density of dislocations ($\sim 10^{14}$ m^{-2}). Within subgrains, quasi-spherical MX precipitates are considered to be randomly dispersed. According to References 6 and 32, the average size of MX particles is around 20-50 nm, with mean interspacing in the order of 300 nm. Larger rod-like $M_{23}C_6$ precipitates (100-300 nm) are located mainly in the grain and subgrain boundaries.

With this microstructure and given the moderate stress range considered in this study, it is foreseen that dislocation motion is arrested at subgrain boundaries (cell walls) and that dislocation transmission across the boundary is unlikely. Recall here that these boundaries contain non-shearable precipitates. In this work, the dislocations are divided into two subsets: subgrain interior dislocations and cell wall dislocations. Plastic deformation is controlled by dislocation glide within subgrains. Those dislocations may be mobilized or immobilized depending on the local stress state and defect content (see Section II–B). Importantly, one notes that subgrains are expected to have a complex stress state due to the dislocations and precipitates they contain. One therefore expects cell walls to exhibit a long-range stress field arising from the primary dislocation network and rod-like precipitates within the subgrain boundaries.

Within subgrains, two types of obstacles to dislocation motion are considered: MX precipitates and other dislocations within the cell. The effective dislocation mobility is determined by their waiting time at both types of obstacles. Stored dislocations can overcome MX precipitates via either a thermally activated glide (junction unzipping and Orowan bypass mechanism for incoherent precipitates) or a climb-assisted glide process depicted in Figure 2. The climb process is non-conservative and therefore is rate limited by the vacancy flux towards or away from the dislocation.[19–22]
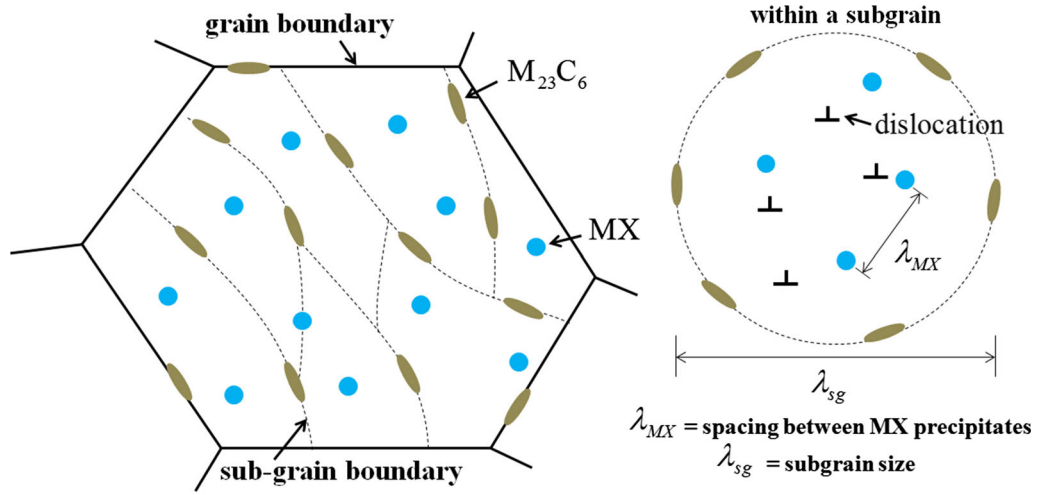
Fig. 1—Schematic view of the microstructure for heat-treated high Cr steels.
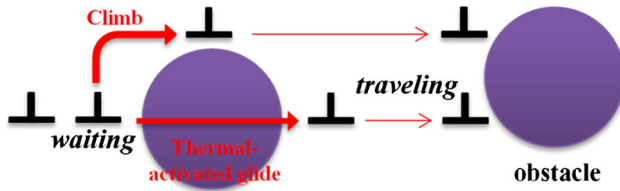

Fig. 2—Schematic view of the obstacle-bypass mechanisms for moving dislocations.

The evolution of the dislocation population within the subgrain is complex as the following processes are simultaneously active: (i) dislocation generation; (ii) dynamic recovery resulting from the short-range interaction with other dislocations; (iii) trapping in the subgrain boundaries. The dislocations population in the cell wall can also reconfigure itself with time. It is postulated here that within cell walls, annihilation due to climb is a dominant feature. Rigorously, the dislocation annihilation in the cell wall should result in a change in the subgrain size, and hence affect the mechanical response.[33,34] However, this process is not considered here due to the lack of related statistical information. In addition, within the temperature and stress regimes considered [873 K to 973 K (600 °C to 700 °C)], ≥80 MPa), diffusion creep and precipitate coarsening are neglected.

B. Constitutive Law

The proposed model deals with the mechanical behavior at material point level. Within the paradigm microstructure, a material point will represent a grain containing a number of subgrains. The stress distribution within a material point is heterogeneous. Theoretically, each material point can be decomposed into infinite sub-material points. The stress state is different at each point depending on the local dislocation arrangement. Some dislocations within the subgrain may be able to overcome the obstacles and keep gliding, whereas others will be immobilized due to the low stress

state acting on them. However, effective medium models such as the VPSC model used in this work determine the inclusion-matrix interaction assuming the state inside of the grain or grain cluster is homogenous. Thus, it is necessary to properly express the mean mechanical behavior considering the response in all sub-material points.

Using a crystal plasticity formalism, the plastic strain rate at the material point scale can be written as the sum of the shear strain rates on all potentially active slip systems as follows:

$$\dot{\varepsilon}_{ij}^{p} = \sum_{s} m_{ij}^{s} \bar{\dot{\gamma}}^{s} \qquad [1]$$

Here $m_{ij}^{s} = \frac{1}{2}\left(n_i^s b_j^s + n_j^s b_i^s\right)$ is the symmetric Schmid tensor associated with slip system s in a material point p; $\mathbf{n}^s$ and $\mathbf{b}^s$ are the normal and Burgers vectors of this system. $\bar{\dot{\gamma}}^s$ denotes the mean shear rate in one material point. Similarly to the approach proposed in References 35 and 36, the latter is given by an integral over all the local shear rates weighted by the volume fraction of the sub-material point. In the calculation, a probability distribution function P is used to represent the volume fraction distribution of sub-material points with a resolved shear stress (τ^s). P is referred to the average resolved shear of the material point ($\bar{\tau}^s$):

$$\bar{\dot{\gamma}}^s = \int_{-\infty}^{\infty} \dot{\gamma}^s(\tau^s) P(\tau^s - \bar{\tau}^s) d\tau^s, \qquad [2]$$

where $\bar{\tau}^s = \boldsymbol{\sigma} : \mathbf{m}$ with $\boldsymbol{\sigma}$ being the deviatoric stress of the material point. $\dot{\gamma}^s$ represents the shear rate of a sub-material point. P is described by the Gaussian distribution function:

$$P(\tau^s - \bar{\tau}^s) = \frac{1}{\sqrt{2\pi V}} \exp\left(-\frac{(\tau^s - \bar{\tau}^s)^2}{2V}\right) \qquad [3]$$

V is the variance of the resolved shear stress, which is linked to the dislocation density.[35,36] It should be different for each slip system and vary during the
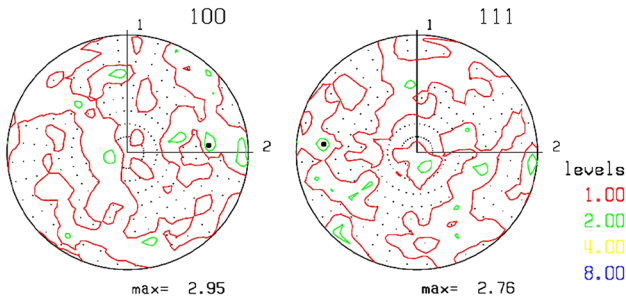
Fig. 3—Pole figures for the initial random texture with 100 grains.

deformation. However, for the sake of simplicity, we assume V is equal for all systems since the initial dislocation arrangement is not completely known. Moreover, V is considered as constant throughout the creep tests. The decrease of dislocation density during creep will lead to a lower V value, and hence will further reduce the shear rate. However, this effect is out of the scope of the present work. In the proposed model, the creep strain is accumulated due to the motion of the dislocations in the interior of the subgrains. The shear rate at each sub-material point can be expressed by the Orowan's equation as:

$$\dot{\gamma}^s = \rho_{\text{cell}}^s b v^s \cdot \text{sign}(\bar{\tau}^s), \qquad [4]$$

where ρ_{cell}^s is the density of dislocations within the subgrains, b is the magnitude of the Burgers vector, and v^s is the mean velocity of dislocations traveling between obstacles. The mean dislocation velocity is given by the dislocation mean free path between obstacles λ^s, divided the time spent in this process. The latter includes the time traveling between obstacles t_t^s and the average time a dislocation spends waiting at an obstacle t_w^s [37–39]:

$$v^s = \frac{\lambda^s}{t_t^s + t_w^s} \qquad [5]$$

The presence of multiple types of obstacles leads to a reduction in the mean free path. Here choice is made to express λ^s as the geometric mean of the interspacing for individual obstacles:

$$\frac{1}{\lambda^s} = \frac{1}{\lambda_{\rho,\text{cell}}^s} + \frac{1}{\lambda_{\text{MX}}^s} \qquad [6]$$

with $\lambda_{\rho,\text{cell}}^s$ and λ_{MX}^s denote the dislocation mean free path for dislocation obstacles and MX precipitates, respectively. The obstacle interspacing determination depends on the nature of the barrier. To first order, $\lambda_{\rho,\text{cell}}^s$ is inversely proportional to the hardening contribution of the dislocations in the cell, as $\tau_{\rho,\text{cell}}^s \propto \mu b / \lambda_{\rho,\text{cell}}^s$. To describe the latent hardening associated with dislocation-dislocation interactions between slip systems, the law proposed by Franciosi

and Zaoui,[40] and for which discrete dislocation dynamics simulations have demonstrated the statistical representativeness,[41] is used in this work as:

$$\tau_{\rho,\text{cell}}^s = \mu b \sqrt{\sum_s \alpha^{ss'} \rho_{\text{cell}}^{s'}} \qquad [7]$$

Also one has:

$$\frac{1}{\lambda_{\rho,\text{cell}}^s} = \sqrt{\sum_s \alpha^{ss'} \rho_{\text{cell}}^{s'}} \qquad [8]$$

$\alpha^{ss'}$ is the effective latent hardening matrix. The interspacing for MX precipitates is written in a simple form derived from the geometrical configuration of the obstacles on the slip plane.[22,42,43]

$$\frac{1}{\lambda_{\text{MX}}^s} = h_{\text{MX}} \sqrt{N_{\text{MX}} d_{\text{MX}}} \qquad [9]$$

here h_{MX} is the trapping coefficient for MX precipitate. N_{MX} and d_{MX} denote the number density and size of MX precipitates. This law is appropriate for hard obstacles,[44] such as MX precipitates. Friedel[45] proposed an alternative expression for attractive obstacles on the glide plane, which is more suitable for weak obstacles.

In Eq. [5], the traveling time is given by $t_t^s = \lambda^s / v_t$. Here v_t is the dislocation traveling velocity which is assumed to be equal to the shear wave velocity C_s (independent of the driving force), since the traveling time is negligible compared to the waiting time. It can be determined by $v_t \approx C_s = \sqrt{\mu / \rho_0}$ [39,46] where ρ_0 is the mass density and μ is the shear modulus given by $\mu = 103572 \text{ MPa} - T \cdot 48 \text{ MPa/K}$.[47]

To determine the dislocation average waiting time, we define the theoretical waiting times of thermally activated glide ($t_{w,g}$) and climb ($t_{w,c}$). These two mechanisms, however, occur simultaneously, which can effectively reduce the waiting time. To first order the waiting time at the obstacle type i (other dislocations, $i = \rho$ or MX precipitates, $i = \text{MX}$) within a sub-material point can be expressed using the harmonic mean:

$$\frac{1}{t_{w,i}^s} = \frac{1}{t_{w,g,i}^s} + \frac{1}{t_{w,c,i}^s} \qquad [10]$$

One notes here that a harmonic transition state theory-based treatment could yield more accurate estimates. The mean waiting time of slip system s when both obstacles are considered is given by the average of $t_{w,\rho}^s$ and $t_{w,\text{MX}}^s$, weighted by the probability that the individual type of obstacle is encountered by the moving dislocation:

$$t_w^s = P_\rho t_{w,\rho}^s + (1 - P_\rho) t_{w,\text{MX}}^s \qquad [11]$$

P_ρ is the probability that a dislocation encounters other dislocation and $1 - P_\rho$ that it encounters MX

precipitates. Statistically, the inverse of mean free path represents the number of obstacles per unit length along the gliding direction. In this way, the ratio of dislocation type obstacles in the corresponding section can be determined by the proportion between $1/\lambda_\rho^s$ and $1/\lambda^s$. Connecting with Eqs. [6] through [9], we will have:

$$P_\rho = \frac{1/\lambda_\rho^s}{1/\lambda^s} = \frac{\sqrt{\sum_s \alpha^{ss'}\rho_{\text{cell}}^{s'}}}{\sqrt{\sum_s \alpha^{ss'}\rho_{\text{cell}}^{s'}} + h_{\text{MX}}\sqrt{N_{\text{MX}}d_{\text{MX}}}} \quad [12]$$

1. Thermally activated glide

The thermally activated glide describes the obstacle bypass processes including the unzipping of the junctions and the Orowan mechanism for large size particles. The MX precipitates are incoherent with the matrix and therefore impenetrable. In this case, the bypass at low-stress states is unlikely. However, under high driving stress, the dislocation can bow out between the MX precipitates, merge on the other side of the obstacle and continue to glide. The bypass for both types of obstacles can be considered as thermally activated process. Therefore, $t_{w,g,\text{MX}}^s$ and $t_{w,g,\rho}^s$ can be described using the Kocks-type activation enthalpy law[37,39,48] but with different values for the attempt frequencies and activation energies:

$$\frac{1}{t_{w,g,i}^s} = \frac{v_{G,i}^s}{\exp\left(\frac{\Delta G_i^s}{kT}\right)} \qquad (i = \text{MX or } \rho) \quad [13]$$

In Eq. [13], i refers to different types of obstacles (dislocations or MX precipitates). $v_{G,i}^s$, k, and T are the effective attempt frequency, Boltzmann constant, and absolute temperature, respectively. ΔG_i^s denotes the activation energy given by:

$$\Delta G_i^s = \begin{cases} \Delta G_{0,i}\left(1 - \left(\frac{|\tau^s|}{\tau_c^s}\right)^p\right)^q & \text{if } |\tau^s| < \tau_c^s, \\ 0 & \text{if } |\tau^s| \geq \tau_c^s \end{cases} \quad [14]$$

where $\Delta G_{0,i}$ is activation energy without any external stress applied. Its value is dependent on the nature of the obstacle, such as the dislocation interaction and the strength and size of precipitates. p ($0 < p \leq 1$) and q ($1 \leq p < 2$) are the exponent parameters in the phenomenological relation determining the shape of the obstacles resistance profile.[48] τ_c^s is the critical resolved shear stress (CRSS). The hardening contributions from the dislocations in the subgrain and MX precipitates, as well as the M$_{23}$C$_6$ precipitates and the dislocations in the cell wall due to the long-term stress field. The long-range hardening induced by multiple sources has been studied in many works i.e., References 42, 49, and 50. A commonly used superposition principle is written as:

$$\tau_t^m = \tau_1^m + \tau_2^m \quad [15]$$

τ_1 and τ_2 are the hardening due to source 1 and 2, respectively. τ_t denotes the superimposed hardening. The exponent m varies between 1 and 2 depending on the hardening mechanisms. A value higher than 2 is reported for irradiation-induced defects.[42] The long-range hardening sources within the microstructure paradigm include the MX precipitates, M$_{23}$C$_6$ carbides, and the dislocations. Notice that the dislocations comprise two populations: the ones within the subgrain cell (ρ_{cell}) and the ones in cell wall (ρ_{cw}). Both of them contribute to the hardening due to the long-range stress field with similar features. Consequently, it is reasonable to consider them as one individual hardening source. As mentioned above, the hardening due to dislocation can be obtained using the complex form of the Taylor law:

$$\tau_\rho^s = \mu b \sqrt{\sum_s \alpha^{ss'}\left(\rho_{\text{cell}}^{s'} + \rho_{\text{cw}}^{s'}\right)} \quad [16]$$

The precipitate hardening should superimpose with τ_ρ^s using the principle in Eq. [15]. Moreover, the linear superimposition is restricted if one of the hardening sources is the intrinsic frictional resistance τ_0^s.[42,49,50] Therefore, the total CRSS is given by:

$$\tau_c^s = \tau_0^s + \left(\left(\tau_\rho^s\right)^m + \left(\tau_P^s\right)^m\right)^{1/m} \quad [17]$$

τ_P^s is the hardening contributions by both MX and M$_{23}$C$_6$ precipitates.

In this work, the attempt frequency for overcoming an MX precipitate is assumed to be constant. The one for junction unzipping process $v_{G,\rho}$ is suggested to be dependent on the dislocation traveling velocity, an entropy factor χ (of the order of 1) and the average length of the vibrating dislocation segments (represented by the dislocation mean free path λ^s).[36,51]

$$v_{G,\rho} = \chi C_s/\lambda^s \quad [18]$$

2. Dislocation climb

Dislocation climb refers to the process that edge dislocations migrate perpendicular to the slip plane via point defect absorption/emission. This stress- and temperature-dependent mechanism may assist the edge dislocations to bypass the barriers during deformation. The effects of climb are more evident at high-temperature due to the high concentration and diffusivity of point defects.[19–22] In the present work, the concept of climb waiting time (Eq. [10]) is introduced to describe this process. Notice that the activation of climb process will affect the mean dislocation mobility, but the sign of shear rate is only governed by the resolved shear stress, which captures the fact that the climb mechanism is assisting the dislocation glide.

Several modeling works have focused on the case of dislocation climb.[18,22,46,52–55] From the physics standpoint, the climb velocity depends on the climb driving

force and on the flow of point defects into the edge dislocations. The climb component of Peach-Koehler force has been discussed in References 56 through 60 and is essential to determine the climb rate on each slip system in a crystallographic framework. Notice that climb may be a reaction-rate-controlled process or a diffusion-controlled process.[18] The former usually occurs in irradiated materials, where the current of defects entering and/or leaving the dislocation core are very large and reach the defect-dislocation reaction rate limit. Otherwise, climb is a diffusion-controlled process, such as in the thermal creep case. Some authors[18,46,52–55] determine the flux of vacancies through the gradient of the vacancy concentration in the dislocation control volume. The detailed description of this method is given in the Appendix. The net current of vacancies I_v^s for slip system s can be expressed as:

$$I_v^s = \frac{2\pi b D_v \left[C_v^\infty - C_v^0 \exp\left(\frac{-f_c^s \Omega}{kTb} \right) \right]}{\Omega b \ln(r_\infty/r_d)} \quad [19]$$

here $\Omega \approx b^3$ is the atomic volume. D_v is the vacancy diffusivity. C_v^0 is the equilibrium vacancy concentration at temperature T in the bulk of the crystal, given by $C_v^0 = \exp\left(S_f^v/k \right) \exp\left(-E_f^v/kT \right)$.[18] E_f^v and S_f^v are the vacancy formation energy and entropy, respectively. C_v^∞ represents the vacancy concentration in the material matrix which is assumed to be equal to C_v^0 in the present work. f_c^s is the climb component of Peach–Koehler force.[56–60] r_d and r_∞ denote the radii of the inner and outer boundaries for the cylindrical control volume defined around the dislocation line. Therefore, the climb velocity is given by:

$$v_c^s = \frac{I_v^s \Omega}{b} = \frac{2\pi D_v \left[C_v^\infty - C_v^0 \exp\left(\frac{-f_c^s \Omega}{kTb} \right) \right]}{b \ln(r_\infty/r_d)} \quad [20]$$

The waiting time for climb can be determined by the ratio between the mean climb velocity of the edge dislocation and the average distance to climb before the bypass.[22] In the present work, dislocation climb is assumed to occur for the bypass of both dislocation and MX precipitate obstacles. Therefore, the average waiting time of climb for edge dislocation can be expressed as:

$$\frac{1}{t_{w,c,i}^s} = R_e \frac{|v_c^s|}{l_i} \quad [21]$$

The absolute value of v_c^s is used here because a dislocation can climb over the obstacle in both positive and negative directions. l_i represents the average climb distance to bypass the obstacles. R_e, denoting the proportion of edge dislocations, is introduced since only edge dislocations contributes to the climb process. In BCC structures, the nucleation of the double kink structure is frequent. The motion of the edge (or screw) dislocations will result in the elongation of the screw (or edge) dislocation kinks.[46,61] Since the edge dislocations

glide much faster in BCC material, the density of edge dislocations is usually limited. In this work, $R_e = \rho_{edge}/\rho = 10$pct is estimated.

Arzt *et al.*[19,20] studied the attractive interaction between the climbing dislocation and particles, as a results of which, the edge dislocations may still be attached to the hard particles after the climb-over process. An extra detachment process is required before it can continue to glide. However, this is not included in the proposed model since for the Fe-Cr alloy this process has not been studied in detail. Consequently, the climb rate for the precipitate obstacles may be overestimated in this work.

C. Dislocation density law

The dislocation density evolution plays a key role in the present thermal creep model. The variance of strain rate for the modified 9Cr-1Mo steel is mainly controlled by the evolution of the dislocation density in the subgrain.[4] The dislocation density evolution processes considered in this model for $\dot{\rho}_{cell}^s$ are dislocation generation ($\dot{\rho}_{cell,g}^{s,+}$), dynamic recovery due to multiple mechanisms ($\dot{\rho}_{cell,a}^{s,-}$), and trapping at the cell walls ($\dot{\rho}_{cell,trap}^{s,-}$):

$$\dot{\rho}_{cell}^s = \dot{\rho}_{cell,g}^{s,+} - \dot{\rho}_{cell,a}^{s,-} - \dot{\rho}_{cell,trap}^{s,-} \quad [22]$$

The dislocation generation process concerns the expansion of the pinned dislocation segments. The generation rate is related to the area swept by the moving dislocations. The term $\dot{\rho}_{cell}^{s,+}$ is determined by a commonly used expression[62–64]:

$$\dot{\rho}_{cell,g}^{s,+} = \frac{k_1}{b\lambda^s} |\dot{\bar{\gamma}}^s| \quad [23]$$

The dynamic recovery process involves many mechanisms. The most important ones are suggested to be cross-slip and climb.[24,65] The moving dislocation can cross-slip and annihilate if it encounters a dislocation with opposite Burger vector. In the classic Kocks-Mecking law,[65–68] the dynamic recovery term can be written as:

$$\dot{\rho}_{cell,a}^{s,-} = f\rho_{cell}^s |\dot{\bar{\gamma}}| \quad [24]$$

here f is the recovery parameter. It is suggested to be a function of temperature and strain rate.[65–68] In many works addressing plastic deformation with high applied stress, *i.e.*, Referenes 64 and 68 this parameter is considered as weakly dependent on the strain rate (or completely insensitive). Estrin[65] indicated that the strain rate sensitivity of f is in fact associated with the dominant mechanism. Compared to cross-slip, the f parameter should be more sensitive to strain rate in the climb governed process. Estrin[65] also proposed a general expression for f as:

$$f = k_2 \left(\frac{\dot{\varepsilon}_0}{\dot{\varepsilon}} \right)^{\frac{1}{n_0}} \quad [25]$$

where $\dot{\varepsilon}_0$ is a reference strain rate and n_0 is related to the strain rate sensitivity. The value of n_0 should be around 3-5 for high temperature cases (climb dominated recovery), or higher in low temperature regime where recovery is mainly controlled by cross-slip.[65] Using a geometric reasoning, moving dislocation may be immobilized after it swept a certain area.[22,39,69] Therefore, the trapping term in the present model is given by:

$$\dot{\rho}_{\text{cell,trap}}^{s,-} = \frac{k_3}{\lambda_{sg}} |\bar{\dot{\gamma}}|, \qquad [26]$$

where λ_{sg} represents the sub-grain size. As mentioned in Section II–A, λ_{sg} is assumed to be constant throughout the creep test in this work. In Eqs. [23] through [26], k_1, k_2, and k_3 are material constants.

The evolution of the dislocation density in the cell wall is determined through the trapping of the moving dislocations and the annihilation process, written as:

$$\dot{\rho}_{\text{cw}}^s = \dot{\rho}_{\text{cell,trap}}^{s,-} - \dot{\rho}_{\text{cw},a}^{s,-} \qquad [27]$$

Different from the dynamic recovery in Eqs. [24] and [25], the annihilation in the cell wall is only controlled by climb since the trapped dislocations cannot glide.[27] Nes[24] suggested that the climb-only annihilation rate is proportional to the dislocation climb velocity and current dislocation density, and inversely proportional to the average dipole separation (l_g) as $\dot{\rho}_{\text{climb}}^{s,-} \propto \rho^s |v_c^s| / l_g$. l_g scales with $1/\sqrt{\rho_{\text{cw}}^{s,-}}$. Therefore:

$$\dot{\rho}_{\text{cw},a}^{s,-} = k_c |v_c^s| (\rho_{\text{cw}}^s)^{\frac{3}{2}} \qquad [28]$$

k_c is a material constant and the climb velocity v_c^s is given in Eq. [20].

D. Brief Description of VPSC Model

The detailed description of VPSC model can be found in References 31 and 70. In this work, the VPSC framework is used as a platform for calculating the interaction between the effective medium representing the macroscopic polycrystal and the individual grains. The self-consistent model treats each grain as an inhomogeneous visco-plastic inclusion embedded in the "homogeneous effective medium" (HEM). Deformation takes place either by enforcing a macroscopic deformation rate or imposing a stress for prescribed time increment. The latter case corresponds to creep. The total strain rate in one grain is given by the sum of the shear rates of all systems (Eq. 1). Its linearized form is written as:

$$\dot{\varepsilon}_{ij}^g = M_{ijkl}^g \sigma_{kl} + \dot{\varepsilon}_{ij}^{0,g}, \qquad [29]$$

where M_{ijkl}^g and $\dot{\varepsilon}_{ij}^{0,g}$ are the visco-plastic compliance and the back-extrapolated rate of grain g, respectively. M_{ijkl}^g should be calculated as[35]:

$$M_{ijkl}^g = \frac{\partial \dot{\varepsilon}_{ij}^g}{\partial \sigma_{kl}} = \sum_s \frac{\partial \bar{\dot{\gamma}}}{\partial \bar{\tau}^s} \frac{\partial \bar{\tau}^s}{\partial \sigma_{kl}} m_{ij} = \sum_s \frac{\partial \bar{\dot{\gamma}}}{\partial \bar{\tau}^s} m_{ij} m_{kl} \qquad [30]$$

Similar to Eq. [29], the relationship between the strain rate and stress for the aggregate is expressed as a linearized form:

$$\bar{\dot{\varepsilon}}_{ij} = \bar{M}_{ijkl} \bar{\sigma}_{kl} + \bar{\dot{\varepsilon}}_{ij}^0 \qquad [31]$$

with $\bar{\dot{\varepsilon}}_{ij}$, $\bar{\sigma}_{kl}$, $\bar{M}_{ijkl}$, and $\bar{\dot{\varepsilon}}_{ij}^0$ denoting the macroscopic strain rate, stress, visco-plastic compliance tensor, and back-extrapolated rate, respectively. The interaction between the single crystal and the surrounding effective medium in the VPSC model is expressed in the interaction law:

$$\dot{\varepsilon}_{ij}^g - \bar{\dot{\varepsilon}}_{ij} = -\tilde{M}_{ijkl} (\sigma_{kl}^g - \bar{\sigma}_{kl}) \qquad [32]$$

The interaction tensor $\tilde{M}_{ijkl}$ takes into account the grain shape effect via the Eshelby tensor S as:

$$\tilde{M}_{ijkl} = (I - S)_{ijmn}^{-1} S_{mnpq} \bar{M}_{pqkl}. \qquad [33]$$

III. SIMULATION RESULTS AND DISCUSSION

The experimental data used to evaluate the proposed model are provided by Basirat et al.[14] for the modified Fe-9Cr-1Mo alloy. Prior to the creep tests, this material has been normalized at 1311 K (1038 °C) for 4 hours and tempered at 1061 K (788 °C) for 43 minutes. The resulting microstructure (initial status for the tests) is consistent with the chosen paradigm (see Section II–A). The detailed description can be found in Reference 13 from the same group.

A. Parameter Calibration and Simulation Conditions

The parameters involved in the simulations are discussed in this section. The affine interaction in the VPSC framework is used in this work. The average size of MX precipitates reported in Reference 13 is around 37 nm. The precipitate number density and trapping parameter are chosen to be 3×10^{20} m^{-3} and 1, respectively. This leads to the mean spacing $\lambda_{\text{MX}}^s = 1/h_{\text{MX}} \sqrt{N_{\text{MX}} d_{\text{MX}}} \approx 300$ nm. This value is in the reasonable range according to Reference 6. In the hardening law, the dislocation-dislocation interaction parameters $\alpha^{ss'}$ are chosen based on the data in Reference 71. The hardening superposition factor m is set to 2 as given in References 42, 49, and 50. In the Kocks type law (Eqs. 13 and 14), the parameter $\Delta G_{0,\rho}$, $\Delta G_{0,\text{MX}}$, $\upsilon_{G,\text{MX}}$, p, and q are obtained by back fitting the experimental data within reasonable ranges ($\upsilon_{G,i} \approx 10^{10} - 10^{11}$ s^{-1};[22] $0 < p \leq 1$ and $1 \leq p < 2$[48]). The lattice friction stress τ_0^s is in general a function of temperature. However, according to Gilbert et al.,[72] in Fe, this stress decreases with increasing temperature and vanishes at 700 K (427 °C). Therefore, for the temperature interval studied in this work, which is above 873 K (600 °C), τ_0^s is set to be 0.

In this work, the initial values of ρ^s_{cell} and ρ^s_{cw} for each system are chosen to be 4×10^{12} m^{-2} and 1×10^{13} m^{-2}, respectively. Hence, the densities in the cell and in the cell wall start at 9.6×10^{13} m^{-2} and 2.4×10^{14} m^{-2}, respectively. In this way, the total dislocation density is of the order 10^{14} m^{-2} and the one in the cell wall is higher than that in the cell, which agrees with the experimental observations.[14,73–75] The evolution-related parameters k_1, k_2, k_3, and k_c are calibrated according to the experimental data. The strain rate sensitivity parameter n_0 in the dislocation dynamic recovery term depends on the annihilation mechanisms.[65] Its value is chosen to be 3.5 in this work and the rationality will be discussed in the following sections.

The vacancy diffusivity and the equilibrium concentration of vacancies are important parameters affecting the climb process. They are determined using molecular dynamics simulation data reported by Mendelev and Mishin[76] for BCC Fe. The diffusivity is calculated by:

$$D_v = D_v^0 \exp\left(-E_m^v/kT\right), \quad [34]$$

where the vacancy migration energy E_m^v is 0.6 eV and the diffusion constant D_v^0 is 7.87×10^{-7} m^2/s. The vacancy formation energy and entropy are given as function of temperature:

$$\begin{aligned} E_f^v &= g_0 - g_2 T^2 - 2g_3 T^3 \\ S_f^v &= -g_1 - 2g_2 T - 3g_3 T^2 \end{aligned} \quad [35]$$

The g_x coefficients and the other parameters involved in the calculation of dislocation waiting time are listed in Table I.

Since the cladding material exhibits a weak texture, an initial texture consisting of 100 random orientations (Figure 3) is utilized as input. The $\{110\}\langle 111\rangle$ and $\{112\}\langle 111\rangle$ slip modes are assumed to be active in BCC Fe-Cr-Mo steel. The tensile creep tests are simulated under stress-controlled boundary conditions: stress along axis 3 (Σ_{33}) is imposed and the rest of the stress components Σ_{ij} are enforced to be zero.

The experimental data used to adjust and benchmark the proposed model are taken from available literature.[14] The same temperatures and creep stresses will be applied in the simulations. The results will be presented in Section III–C. Notice that only the primary creep stage and steady-state stage of thermal creep will be simulated. The third stage, where the creep rate shows an evident increase, is usually attributed to void nucleation and crack formation[41,77] and is out of the scope of the present modeling framework.

B. Simulation Results

The creep rate and the creep strain in Basirat et al.[14] are measured under the following conditions: 873 K (600 °C) with 150 and 200 MPa; 923 K (650 °C) with 150 and 200 MPa; 973 K (700 °C) with 80, 100, 150, and 200 MPa. Figures 4 through 7 show the comparison of the predicted results with experiments as a function of stress and temperature. The most obvious feature in these experiments is the strong dependence of the creep rate with applied stress. Differences of 50 MPa or even 20 MPa impact strongly on the creep rates observed. Despite such demanding experimental conditions, reasonable agreement is obtained for both. Notice that the experimental data in Basirat et al. show an obvious power-law regime behavior.[13,14] Therefore, the diffusion creep, which is excluded from this model, will not evidently affect the prediction in this work.

It can be seen that the simulation results capture the evolution for both the creep rate and creep strain curves over a wide range of orders of magnitudes. Still, some discrepancies are apparent in Figures 4 through 7, the possible causes for which are discussed in what follows. First, a random texture is used in this work due to the lack of experimental texture data. Another possible source of error could be the initial dislocation densities used, which are the same for all tests in this work. However, they are likely to be different depending on the temperature, which will induce some annealing. The parameters controlling the waiting time of the thermal-activated glide and climb, could also affect the predicted results. These parameters can be better calibrated using the data from more systematic experiments or low scale dislocation dynamic simulations.

C. Relative Contribution of Glide and Climb Mechanisms

The proposed modeling framework is able to consider the contribution of both the thermally activated glide and the dislocation climb mechanisms in the deformation process. In order to study their relative activities, we define $P_c = 1 - \dot{\varepsilon}^i_{w/o}\big/\dot{\varepsilon}^i_w$ to describe the percentage of the climb contribution. $\dot{\varepsilon}^i_w$ and $\dot{\varepsilon}^i_{w/o}$ denote the creep rates at the initial step of the simulations with and without considering the climb mechanism (using the parameters of Fe-Cr-Mo steel given in Section III–A).

Figure 8 exhibits the predicted relative contribution of climb under various temperature and stress. As shown in Figure 8(a), the contribution of climb is relatively larger at lower temperature. In this model, the climb process is controlled by the temperature-dependent equilibrium vacancy concentration, vacancy diffusivity, and the chemical force (see Appendix). Thermally activated glide is also strongly dependent on temperature. The results in Figure 8(a) indicate that the thermally activated glide is relatively more sensitive to temperature than climb. Figure 8(b) demonstrates that the relative activity of climb is inversely proportional to the creep stress. It can be explained as that the activity of thermally activated glide shows an exponential growth with the stress (Eq.13). On the other hand, the value of $f_c^s\Omega/kTb$ in Eqs. [19] and [20] is low (close to zero). This mathematically leads to a relatively more linear relationship between the climb velocity and the applied stress.[54]

Table I.   Parameters Used for the Fe-Cr-Mo Alloy in This Work

Parameters	Fe-Cr-Mo	
ρ_0 (mass density)	8000 Kg/m^3	
b (magnitude of Burgers vector)	2.48×10^{-10} m	
μ (shear modulus)	103572 MPa-$T \cdot$48 MPa/K	47
N_{MX} (number density of MX precipitate)	3×10^{20} m^{-3}	6*
D_{MX} (average diameter of MX precipitate)	37 nm	13
h_{MX} (trapping coefficient for MX precipitates)	1	6*
τ_0 (friction stress)	0 MPa	72
τ_P^s (hardening contribution of MX precipitates)	365 Mpa for 873 K (600 °C)	
	325 Mpa for 923 K (650 °C)	
	315 Mpa for 973 K (700 °C)	
m (exponent factor)	2	42,49,50
$\alpha_0^{ss'}$ (saturation dislocation-dislocation interaction)	0.7 ($s = s'$); 0.05 ($s \neq s'$)	71*
V (resolved shear stress variance)	1000 MPa^2	
$\Delta G_{0,\rho}$ (zero-stress activation energy for dislocations)	2.8 eV	
$\Delta G_{0,MX}$ (zero-stress activation energy for MX precipitates)	7 eV	
p (exponent parameter)	0.7	48*
q (exponent parameter)	1.4	48*
$v_{G,MX}$ (attack frequency for MX precipitate obstacle)	1.2×10^{10} s^{-1}	22*
R_e (proportion of edge dislocations)	10 pct	
χ (entropy factor)	1	36
r_d (inner radius of dislocation control volume)	$4b$	52
r_∞ (inner radius of dislocation control volume)	$200b$	
$\rho_{cell,0}^s$ (initial dislocation density in the cell)	4×10^{12} m^{-2}	14,73–75*
$\rho_{cw,0}^s$ (initial dislocation density in the cell wall)	1×10^{13} m^{-2}	14,73–75*
l_ρ (average distance to climb for dislocation obstacle)	$100b$	
k_1 (material constant)	0.12	
k_2 (material constant)	85	
k_3 (material constant)	0.5×10^9	
k_c (material constant)	0.1	
λ_{sg} (sub-grain size)	0.5×10^{-6} m	73
n_0 (annihilation strain rate sensitivity)	3.5	
D_v^0 (diffusion constant)	7.87×10^{-7} m^2/s	76
E_m^v (vacancy migration energy)	0.6 eV	76
g_0 (coefficient used in Eq. [35])	1.724 eV	76
g_1 (coefficient used in Eq. [35])	-1.2×10^{-4} eV/K	76
g_2 (coefficient used in Eq. [35])	-2.79×10^{-8} eV/K^2	76
g_3 (coefficient used in Eq. [35])	-5.93×10^{-11} eV/K^3	76

* Parameter estimated or back-fitted from experimental data within the range given in the listed references.
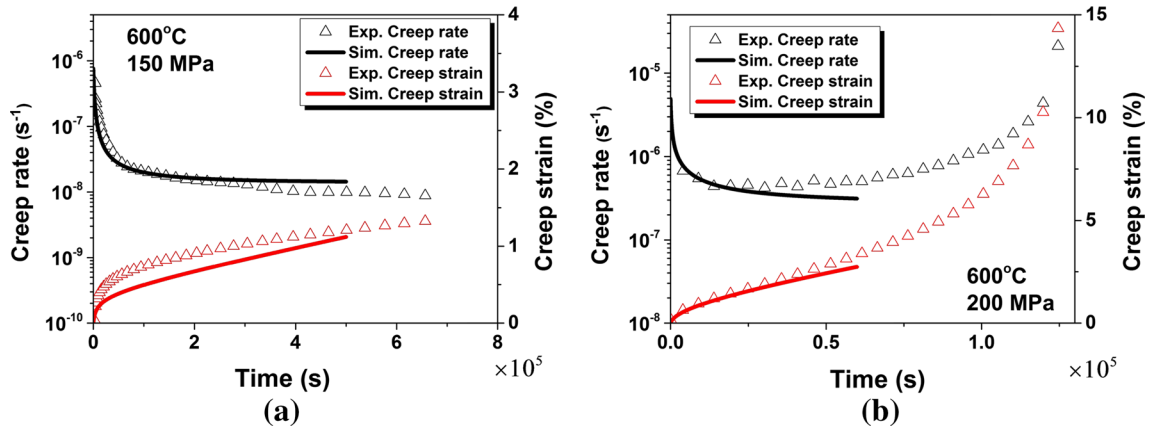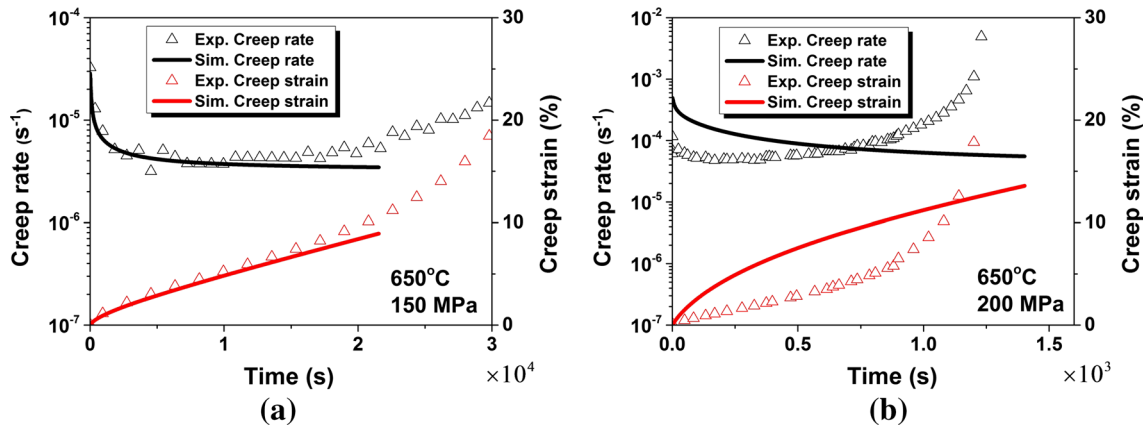

Fig. 4—Predicted creep rate and creep strain for Fe-Cr-Mo steel at 873 K (600 °C) with applied stress of 150 (*a*) and 200 MPa (*b*). Experimental data from Ref. [14].

D. Dislocation Density Evolution

The predicted dislocation density evolutions in the subgrain are presented in Figure 9. The results are compared at various loading condition. It shows that ρ_{cell} tends to decrease more for lower temperature and/or stress. On the other hand, the evolution of ρ_{cw},

Fig. 5—Predicted creep rate and creep strain for Fe-Cr-Mo steel at 923 K (650 °C) with applied stress of 150 (*a*) and 200 MPa (*b*). Experimental data from Ref. [14].
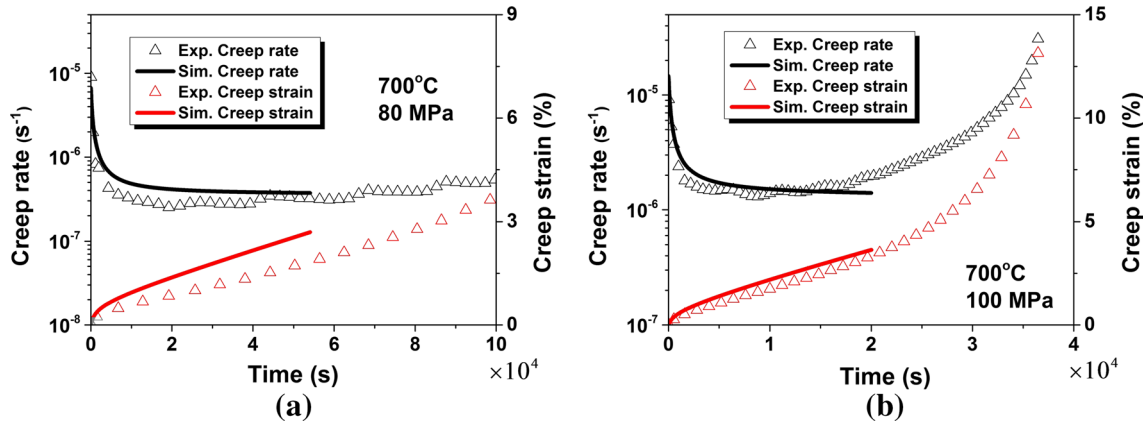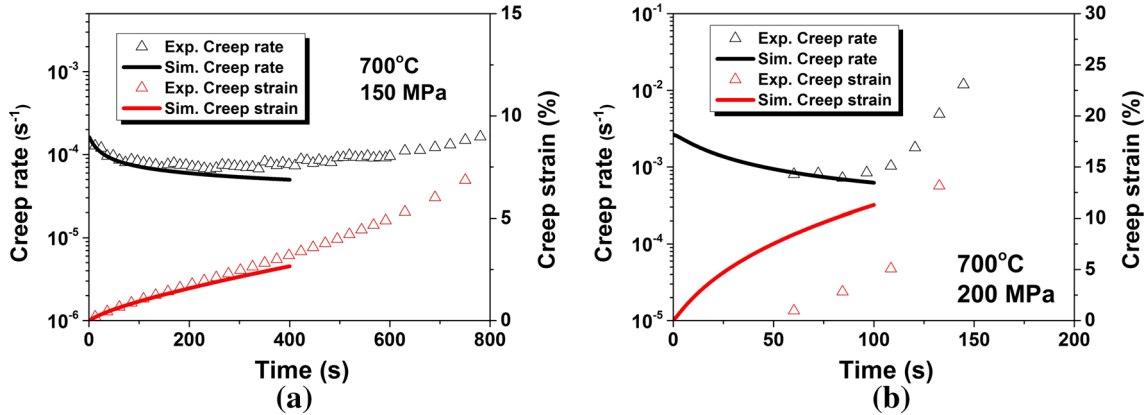

Fig. 6—Predicted creep rate and creep strain for Fe-Cr-Mo steel at 973 K (700 °C) with applied stress of 80 (*a*) and 100 MPa (*b*). Experimental data from Ref. [14].

Fig. 7—Predicted creep rate and creep strain for Fe-Cr-Mo steel at 973 K (700 °C) with applied stress of 150 (*a*) and 200 MPa (*b*). Experimental data from Ref. [14].

given in Figure 10, shows the same tendency. Notice that the subgrain size, which is considered constant in this work, is actually dependent on ρ_{cw}. It has been reported that the saturation subgrain size, which scales with $1/\sqrt{\rho_{cw}}$, is inversely proportional to the applied

stress.[6] This is in agreement with the present simulations.

In Figure 11, the roles of each dislocation density evolution term ($\dot{\rho}_{cell,g}^{s,+}$, $\dot{\rho}_{cell,a}^{s,-}$, $\dot{\rho}_{cell,trap}^{s,-}$ and $\dot{\rho}_{cw,a}^{s,-}$) are analyzed. By summing the components from individual
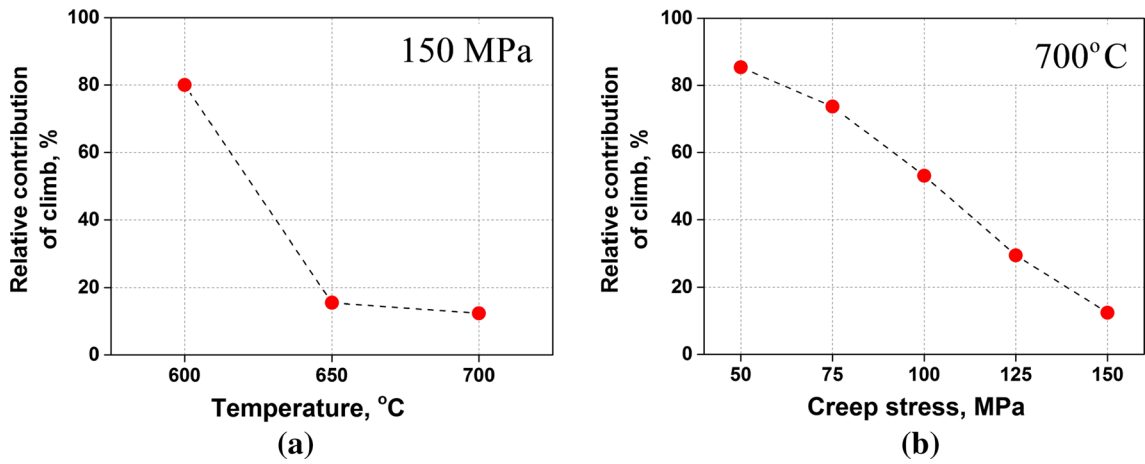
Fig. 8—Relative contribution of dislocation climb mechanism as a function of (*a*) temperature and (*b*) creep stress.
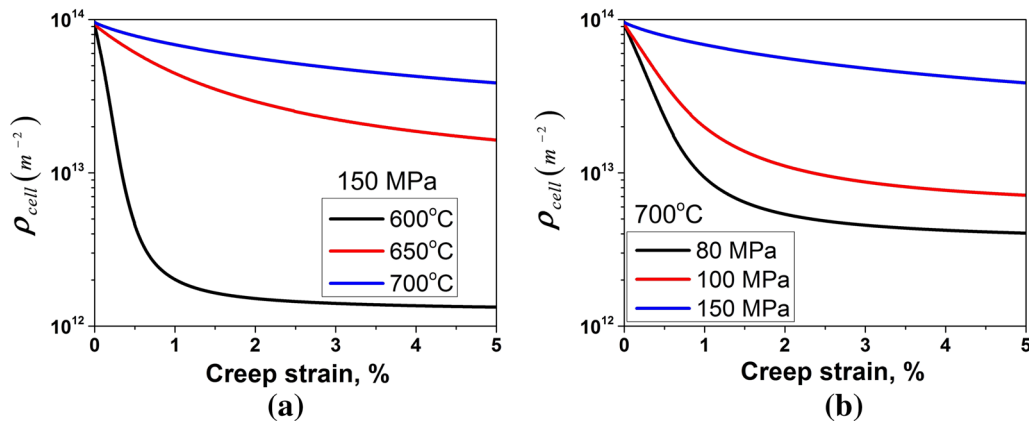

Fig. 9—Predicted evolution of dislocation density within subgrains under different temperatures (*a*) and stresses (*b*).
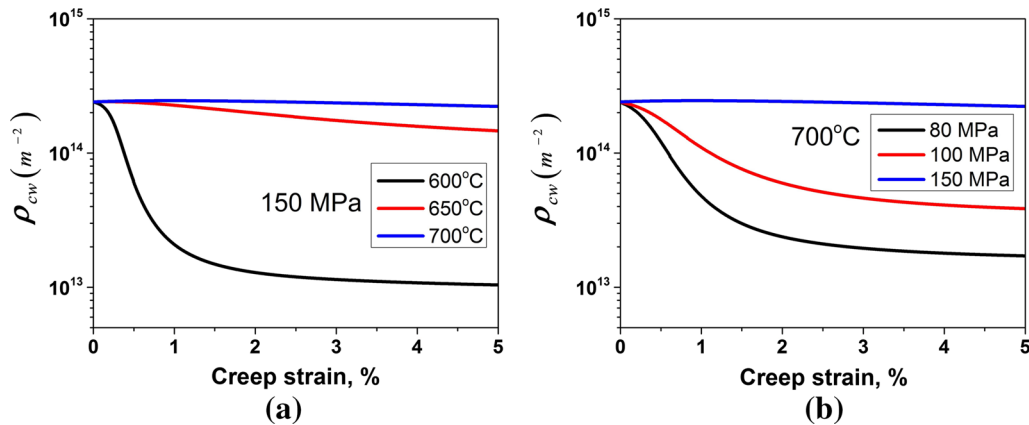

Fig. 10—Predicted evolutions of dislocation density in the cell walls under different temperatures (*a*) and stresses (*b*).

slip systems and then averaging these values across all grains, the macroscopic $\dot{\rho}_{cell,g}^{+}$, $\dot{\rho}_{cell,a}^{-}$, $\dot{\rho}_{cell,trap}^{-}$, and $\dot{\rho}_{cw,a}^{-}$ are calculated for the polycrystal. For lower stress and temperature cases, we can see that the value for $\dot{\rho}_{cell,a}^{-}$ is relatively high at the beginning of the tests. This indicates that the dynamic recovery process dominates the drop of ρ_{cell} (and hence the creep rate) in the primary creep regime.

This term later becomes very weak in the steady state due to the large decrease of ρ_{cell} and creep rate.

The experimental data used in this work[14] show an important dependence of the creep rate evolution with stress and temperature. In Figure 12, some of the experimental creep rate curves are presented for different stresses and temperatures. The strain rate data are
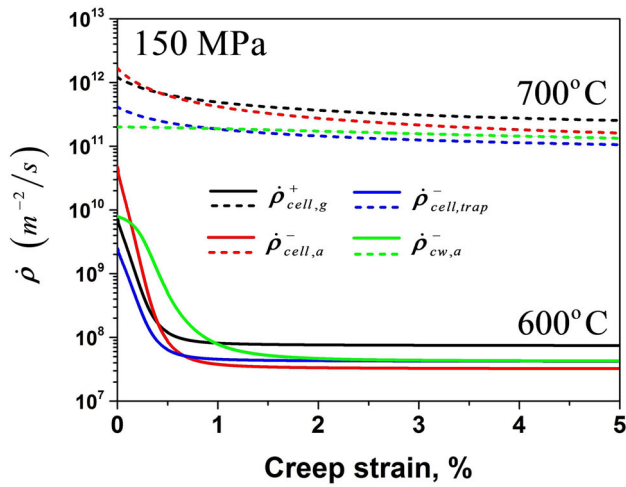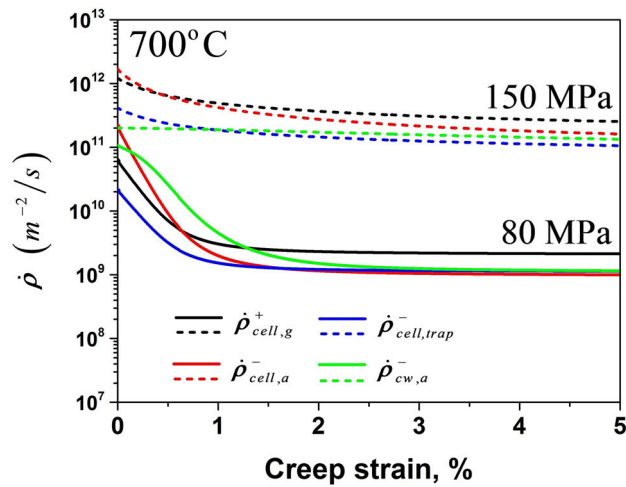
Fig.11—Contribution for the dislocation density evolution-related mechanisms for different temperatures (*a*) and stresses (*b*).

Fig. 12—Experimental creep rate evolution under different stresses and temperatures. Creep rate and time normalized by the initial creep rate and the time that the minimum creep rate presents, respectively. Experimental data from Ref. [14].

normalized by the initial strain rate in the experimental data $\dot{\varepsilon}^i_{\exp}$, whereas the time is normalized by $t_{\min}$, the time where the experimental minimum creep rate appears. Although the initial creep rate is not accurately indicated by experiments, we can see that $\dot{\varepsilon}$ tends to decrease by a larger fraction when a lower stress or temperature is applied. As presented in Figure 13(a), such behavior is reproduced by the proposed model. Here the predicted strain curves (using the parameters listed in Table I) are normalized by the strain rate at the first step of the simulations.

In the proposed model, the dynamic recovery process plays a key role in the evolution of dislocation population in the subgrain, which is responsible for capturing the tendency in experiments. Eq. [25] shows that dynamic recovery is a function of strain rate with sensitivity is governed by n_0. According to Estrin,[65] n_0 should be a constant (around 3-5) for high temperature cases where climb is the dominant mechanism in dynamic recovery. For low temperature cases (cross-slip controlled process), its value should be much higher (of
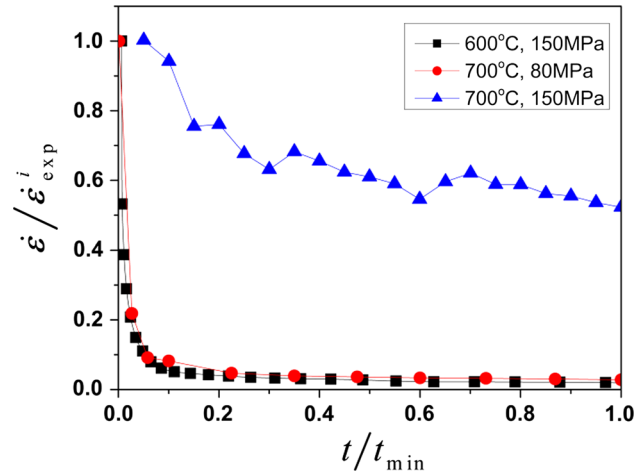
order 20 as in Reference 78). The boundary between the two temperature regimes is not clear and is supposed to vary depending on the material. In this work, $n_0 = 3.5$ is used in the simulations. Otherwise, the strain rate evolution in cannot be captured accordingly with experimental data. In Figure 13(b), the simulation is carried out using $n_0 = 20$ and the parameter k_2 is set to 600 to fit the reference experimental results (973 K (700 °C) and 150 MPa). It shows that the predicted strain rate does not vary evidently under different loading conditions. This result implies dislocation climb is the dominant mechanisms for dynamic recovery process in the conducted creep tests.

As mentioned in Section II–A, the growth of MX and $M_{23}C_6$ precipitates is neglected in this model, as well as the precipitation of Laves-phase and Z-phase. We believe this should not affect the results in the present simulations. The experimental results in Basirat *et al.*[14] correspond to short-term creep tests with a total creep time less than 200 hours. A rough estimate from the data in Reference 7 indicates that the size of MX and $M_{23}C_6$ precipitates will grow less than 0.1 pct within this time range. Moreover, the study of Hayakawa *et al.*[4] shows that the dislocation mobility in modified 9Cr-1Mo steel is not significantly changed during creep tests up to around 7 pct creep strain. This proves indirectly that the microstructure of this material is relatively stable for short-term tests.

IV. CONCLUSIONS AND PERSPECTIVES

In this work, a crystallographic thermal creep model is proposed for Fe-Cr alloy. The thermal-activated glide and climb mechanisms are coupled in the formulation to determine the mean dislocation waiting time at different types of the obstacle (other dislocations and MX precipitates). This model, embedded in the VPSC framework, captures well the thermal creep behavior for modified 9Cr-1Mo steel under various stresses and temperatures.
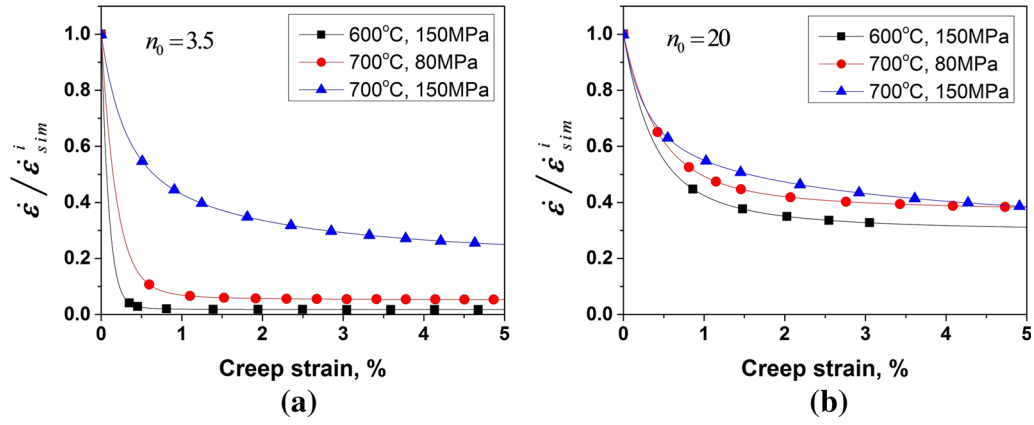
Fig. 13—Predicted creep rate evolution under different stresses and temperatures using (a) $n_0 = 3.5$ and (b) $n_0 = 20$. Creep rate normalized by the initial creep rate.

The relative contribution of thermally activated glide and climb mechanisms is evaluated for different creep conditions. The results show that thermally activated glide is strongly suppressed for creep at lower temperature, but makes a relatively higher contribution on the dislocation mobility in high-stress regime.

The dislocation density evolution law, considering multiple mechanisms in the annihilation process, is also essential to predict correctly the creep behavior for the initial and steady-state stages. The strain rate sensitive dynamic recovery is the dominant factor to capture the strain rate variance under various loading conditions. The dislocation recovery is a sophisticated phenomenon. The physics process is not completely known. The simulation data in this work imply that dislocation climb could be the governing mechanism for the dynamic recovery in modified 9Cr-1Mo steel (within the corresponding stress and temperature intervals). However, more studies are necessary to unravel its specifics in future.

APPENDIX

Previous studies[18,46,52–54] show the climb velocity can be expressed as:

$$v_c^s = \frac{I_v^s \Omega}{b} \quad [A1]$$

To calculate the vacancy current I_v^s, one needs to analyze the stress and vacancy concentration status around the climbing edge dislocation. A cylindrical control volume around the dislocation line with the radius r is defined. The zone with $r \leq r_d$ is considered as the dislocation core region. Therefore the chemical force (Osmotic force) applied on the unit length of edge dislocation segment can be obtained as[46,79]:

$$f_{os}^s = -\frac{kTb}{\Omega} \ln\left(\frac{C_v^s(r_d)}{C_v^0}\right), \quad [A2]$$

where $C^v(r_d)$ represents the vacancy concentration at $r = r_d$. C_v^0 is the equilibrium vacancy concentration at a given temperature.

Meanwhile, climb is also affected by the climb component of Peach-Koehler force. The full Peach-Koehler force is defined as $f = (\boldsymbol{\sigma} \cdot b^s) \times t^s$ where t^s is the normalized tangent to the dislocation line.[56,57] The climb component of f for the edge dislocation can be expressed as[58–60]:

$$f_c^s = f^s \cdot n^s = [(\boldsymbol{\sigma} \cdot b^s) \times t^s] \cdot n^s = -|b^s|\boldsymbol{\sigma} : (b^s \otimes b^s) \quad [A3]$$

When the dislocation is locally in equilibrium state, the total force $f^s = f_{os}^s + f_c^s$ should be equal to 0. Therefore we get from Eqs. [A2] and [A3]:

$$C_v^s(r_d) = C_{v,eq}^s = C_v^0 \exp\left(\frac{-f_c^s \Omega}{kTb}\right) \quad [A4]$$

Notice that the vacancy concentration in the material matrix is assumed to be equal to the equilibrium concentration, $C_v(r \geq r_\infty) = C_v^\infty = C_v^0$, where r_∞ denotes the radius of the outer boundary for the control volume. Therefore, a vacancy concentration gradient along the radius appears in the control volume which leads to a diffusive flow of vacancies. The dislocation needs to absorb or emit vacancies (climb) to retain the local equilibrium status.

At steady-state the divergence of vacancy diffusion flux J is null in the absence of defect creation. The associated Laplace equation in the cylindrical coordinate system is:

$$\nabla^2 C_v^s = \frac{1}{r}\frac{\partial}{\partial r} r \frac{\partial C_v^s}{\partial r} = 0 \quad [A5]$$

with the inner and outer boundary conditions:

$$C_v^s(r = r_\infty) = C_v^\infty = C_v^0$$
$$C^v(r = r_d) = C_{v,\text{eq}}^s \qquad [A6]$$

By solving Eq. [A5], we obtain:

$$C_v^s(r) = C_{v,\text{eq}}^s + (C_v^\infty - C_{v,\text{eq}}^s)\frac{\ln(r/r_\infty)}{\ln(r_\infty/r_d)} \qquad [A7]$$

Therefore, the net current absorbed or emitted by unit length of dislocation segment is given by:

$$I_v^s = 2\pi r \cdot J = 2\pi r \frac{D_v}{\Omega}\frac{\partial C_v^s(r)}{\partial r} = \frac{2\pi D_v\left[C_v^\infty - C_v^0\exp\left(\frac{-f_c^s\Omega}{kTb}\right)\right]}{\Omega\ln(r_\infty/r_d)},$$
$$[A8]$$

where D_v is the vacancy diffusivity. Then the climb velocity can be expressed as:

$$v_c^s = \frac{I_v^s\Omega}{b} = \frac{2\pi D_v\left[C_v^\infty - C_v^0\exp\left(\frac{-f_c^s\Omega}{kTb}\right)\right]}{b\ln(r_\infty/r_d)}. \qquad [A9]$$

REFERENCES

1. Fujio. Abe: *Sci. Technol. Adv. Mater.*, 2008, vol. 9, pp. 13002–15.
2. E. Cerri, E. Evangelista, S. Spigarelli, and P. Bianchi: *Mater. Sci. Eng. A*, 1998, vol. 245, pp. 285–92.
3. H.K. Danielsen: *Mater. Sci. Technol.*, 2015, vol. 836, pp. 126–37.
4. Hiroyuki. Hayakawa, Satoshi. Nakashima, Junichi. Kusumoto, Akihiro. Kanaya, and Hideharu. Nakashima: *Int. J. Press. Vessel. Pip.*, 2009, vol. 86, pp. 556–62.
5. S. Yamasaki: Ph.D. Thesis, University of Cambridge, 2009.
6. K. Maruyama, K. Sawada, and J. Koike: *ISIJ Int.*, 2001, vol. 41, pp. 641–53.
7. Takeshi. Nakajima, Stefano. Spigarelli, Enrico. Evangelista, and Takao. Endo: *Mater. Trans.*, 2003, vol. 44, pp. 1802–08.
8. J. Hald: *Int. J. Press. Vessel. Pip.*, 2008, vol. 85, pp. 30–37.
9. Y. Yamamoto, B.A. Pint, K.A. Terrani, K.G. Field, Y. Yang, and L.L. Snead: *J. Nucl. Mater.*, 2015, vol. 467, pp. 703–16.
10. Kevin.G. Field, Maxim.N. Gussev, Yukinori. Yamamoto, and Lance.L. Snead: *J. Nucl. Mater.*, 2014, vol. 454, pp. 352–58.
11. Kevin.G. Field, Hu. Xunxiang, Kenneth.C. Littrell, Yukinori. Yamamoto, and Lance.L. Snead: *J. Nucl. Mater.*, 2015, vol. 465, pp. 746–55.
12. Triratna. Shrestha, Mehdi. Basirat, Indrajit. Charit, Gabriel.P. Potirniche, and Karl.K. Rink: *Mater. Sci. Eng. A*, 2013, vol. 565, pp. 382–91.
13. Triratna. Shrestha, Mehdi. Basirat, Indrajit. Charit, Gabriel.P. Potirniche, Karl.K. Rink, and Uttara. Sahaym: *J. Nucl. Mater.*, 2012, vol. 423, pp. 110–19.
14. M. Basirat, T. Shrestha, G.P. Potirniche, I. Charit, and K. Rink: *Int. J. Plast.*, 2012, vol. 37, pp. 95–107.
15. M. Tamura, H. Sakasegawa, A. Kohyama, H. Esaka, and K. Shinozuka: *J. Nucl. Mater.*, 2003, vol. 321, pp. 288–93.
16. Masaki. Taneike, Fujio. Abe, and Kota. Sawada: *Nature*, 2003, vol. 424, pp. 294–96.
17. S. Spigarelli, E. Cerri, P. Bianchi, and E. Evangelista: *Mater. Sci. Technol.*, 2016, vol. 15, pp. 1433–40.
18. G.S. Was: *Fundamentals of Radiation Materials Science: Metals and Alloys*, Springer, New York, 2007.
19. E. Arzt and J. Rosler: *Acta Metall.*, 1988, vol. 36, pp. 1053–60.
20. E. Arzt and D.S. Wilkinson: *Acta Metall.*, 1986, vol. 34, pp. 1893–98.
21. J. Roesler and E. Arzt: *Acta Metall.*, 1988, vol. 36, pp. 1043–51.
22. Anirban. Patra and David.L. McDowell: *Philos. Mag.*, 2012, vol. 92, pp. 861–87.
23. Y. Qin, G. Götz, and W. Blum: *Mater. Sci. Eng. A*, 2003, vol. 341, pp. 211–15.
24. Erik. Nes: *Prog. Mater. Sci.*, 1997, vol. 41, pp. 129–93.
25. Y. Estrin and H. Mecking: *Acta Metall.*, 1984, vol. 32, pp. 57–70.
26. G. Gottstein and A.S. Argon: *Acta Metall.*, 1987, vol. 35, pp. 1261–71.
27. F. Roters, D. Raabe, and G. Gottstein: *Acta Mater.*, 2000, vol. 48, pp. 4181–89.
28. Y. Xiang and D.J. Srolovitz: *Philos. Mag.*, 2006, vol. 86, pp. 3937–57.
29. R. Oruganti: *Acta Mater.*, 2012, vol. 60, pp. 1695–1702.
30. R.A. Lebensohn and C.N. Tomé: *Acta Metall. Mater.*, 1993, vol. 41, pp. 2611–24.
31. R.A. Lebensohn, C.N. Tomé, and P.P. CastaÑeda: *Philos. Mag.*, 2007, vol. 87, pp. 4287–4322.
32. B. Fournier, M. Sauzay, and A. Pineau: *Int. J. Plast.*, 2011, vol. 27, pp. 1803–16.
33. László.S. Tóth, Alain. Molinari, and Yuri. Estrin: *J. Eng. Mater. Technol.*, 2002, vol. 124, p. 71.
34. Y. Estrin, L.S. Tóth, A. Molinari, and Y. Bréchet: *Acta Mater.*, 1998, vol. 46, pp. 5509–22.
35. H. Wang, B. Clausen, L. Capolungo, I.J. Beyerlein, J. Wang, and C.N. Tomé: *Int. J. Plast.*, 2016, vol. 79, pp. 275–92.
36. H. Wang, L. Capolungo, B. Clausen, and C.N. Tomé: *Int. J. Plast.*, 2016, DOI:10.1016/j.ijplas.2016.05.003.
37. J.T. Lloyd, J.D. Clayton, R.A. Austin, and D.L. McDowell: *J. Mech. Phys. Solids*, 2014, vol. 69, pp. 14–32.
38. R.J. Clifton: *Shock Waves and the Mechanical Properties of Solids*, Syracuse University Press, Syracuse, NY, 1970, pp. 73–116.
39. Ryan.A. Austin and David.L. McDowell: *Int. J. Plast.*, 2011, vol. 27, pp. 1–24.
40. P. Franciosi and A. Zaoui: *Acta Metall.*, 1982, vol. 30, pp. 1627–37.
41. N. Bertin, C.N. Tomé, I.J. Beyerlein, M.R. Barnett, and L. Capolungo: *Int. J. Plast.*, 2014, vol. 62, pp. 72–92.
42. C. Sobie, N. Bertin, and L. Capolungo: *Metall. Mater. Trans. A*, 2015, vol. 46A, pp. 3761–72.
43. G.E. Lucas: *J. Nucl. Mater.*, 1993, vol. 206, pp. 287–305.
44. C. Deo, C.N. Tomé, R. Lebensohn, and S. Maloy: *J. Nucl. Mater.*, 2008, vol. 377, pp. 136–40.
45. J. Friedel: *Electron Microscopy and Strength of Crystals*, Interscience Publishers, Wiley, New York, 1963, p. 605.
46. J.P. Hirth and J. Lothe: *J. Appl. Mech.*, 1983, vol. 50, p. 476.
47. V. Gaffard: Ph.D. Thesis, Ingénieur de l'Institut National Polytechnique de Grenoble (ENSEEG), 2004.
48. U.F. Kocks, A.S. Argon, and M.F. Ashby: *Prog. Mater. Sci.*, 1975, vol. 19, pp. 171–229.
49. U. Lagerpusch, V. Mohles, D. Baither, B. Anczykowski, and E. Nembach: *Acta Mater.*, 2000, vol. 48, pp. 3647–56.
50. Y. Dong, T. Nogaret, and W.A. Curtin: *Metall. Mater. Trans. A*, 2010, vol. 41A, pp. 1954–60.
51. A.V. Granato, K. Lücke, J. Schlipf, and L.J. Teutonico: *J. Appl. Phys.*, 1964, vol. 35, p. 2732.
52. M.G.D. Geers, M. Cottura, B. Appolaire, E.P. Busso, S. Forest, and A. Villani: *J. Mech. Phys. Solids*, 2014, vol. 70, pp. 136–53.
53. B. Bakó, E. Clouet, L.M. Dupuy, and M. Blétry: *Philos. Mag.*, 2011, vol. 91, pp. 3173–91.
54. Y. Gu, Y. Xiang, S.S. Quek, and D.J. Srolovitz: *J. Mech. Phys. Solids*, 2014, vol. 83, pp. 319–37.
55. D. Mordehai, E. Clouet, M. Fivel, and M. Verdier: *Philos. Mag.*, 2008, vol. 88, pp. 899–925.
56. J. Weertman: *Philos. Mag.*, 1965, vol. 11, pp. 1217–23.
57. J. Weertman and J.R. Weertman: *Elementary Dislocation Theory*, Oxford University Press, Oxford, 1992.
58. R.A. Lebensohn, C.S. Hartley, C.N. Tomé, and O. Castelnau: *Philos. Mag.*, 2010, vol. 90, pp. 567–83.
59. R.A. Lebensohn, R.A. Holt, A. Caro, A. Alankar, and C.N. Tomé: *Comptes Rendus.*, 2012, vol. 340, pp. 289–95.
60. Craig.S. Hartley: *Philos. Mag.*, 2003, vol. 83, pp. 3783–3808.
61. J. Chang, W. Cai, V.V. Bulatov, and S. Yip: *Mater. Sci. Eng. A*, 2001, vols. 309–310, pp. 160–63.

62. W. Wen, M. Borodachenkova, C.N. Tomé, G. Vincze, E.F. Rauch, F. Barlat, and J.J. Grácio: *Acta Mater.*, 2016, vol. 111, pp. 305–14.
63. W. Wen, M. Borodachenkova, C.N. Tomé, G. Vincze, E.F. Rauch, F. Barlat, and J.J. Grácio: *Int. J. Plast.*, 2015, vol. 73, pp. 171–83.
64. K. Kitayama, C.N. Tomé, E.F. Rauch, J.J. Gracio, and F. Barlat: *Int. J. Plast.*, 2013, vol. 46, pp. 54–69.
65. Y. Estrin: *J. Mater. Process. Technol.*, 1998, vols. 80–81, pp. 33–39.
66. U.F. Kocks and H. Mecking: *Prog. Mater. Sci.*, 2003, vol. 48, pp. 171–273.
67. H. Mecking and U.F. Kocks: *Acta Metall.*, 1981, vol. 29, pp. 1865–75.
68. I.J. Beyerlein and C.N. Tomé: *Int. J. Plast.*, 2008, vol. 24, pp. 867–95.
69. U.F. Kocks: *Philos. Mag.*, 1966, vol. 13, pp. 541–566.
70. H. Wang, B. Raeisinia, P.D. Wu, S.R. Agnew, and C.N. Tomé: *Int. J. Solids Struct.*, 2010, vol. 47, pp. 2905–17.
71. S. Queyreau, G. Monnet, and B. Devincre: *Int. J. Plast.*, 2009, vol. 25, pp. 361–77.
72. M.R. Gilbert, P. Schuck, B. Sadigh, and J. Marian: *Phys. Rev. Lett.*, 2013, vol. 111, pp. 1–5.
73. C.G. Panait, A. Zielińska-Lipiec, T. Koziel, A. Czyrska-Filemonowicz, A.-F. Gourgues-Lorenzon, and W. Bendick: *Mater. Sci. Eng. A*, 2010, vol. 527, pp. 4062–69.
74. S. Hollner, B. Fournier, J. Le Pendu, T. Cozzika, I. Tournié, J.C. Brachet, and A. Pineau: *J. Nucl. Mater.*, 2010, vol. 405, pp. 101–8.
75. S.D. Yadav, S. Kalácska, M. Dománková, D.C. Yubero, R. Resel, I. Groma, C. Beal, B. Sonderegger, C. Sommitsch, and C. Poletti: *Mater. Charact.*, 2016, vol. 115, pp. 23–31.
76. M.I. Mendelev and Y. Mishin: *Phys. Rev. B*, 2009, vol. 80, pp. 1–9.
77. V. Gaffard, A.F. Gourgues-Lorenzon, and J. Besson: *Nucl. Eng. Des.*, 2005, vol. 235, pp. 2547–62.
78. J. Li and A.K. Soh: *Int. J. Plast.*, 2012, vol. 39, pp. 88–102.
79. H. Wiedersich and K. Herschbach: *Scr. Metall.*, 1972, vol. 6, pp. 453–57.